RESEARCH PAPER

Biogenic synthesis enhanced structural, morphological, magnetic and optical properties of zinc ferrite nanoparticles for moderate hyperthermia applications

Samson O. Aisida ⬤ · Awais Ali · Oluwole E. Oyewande ·
Ishaq Ahmad · Anwar Ul-Hamid · Ting-kai Zhao ·
M. Maaza · Fabian I. Ezema

Abstract A biogenic protocol has been adopted for the formulation of zinc ferrite nanoparticles (ZFNPs) using an aqueous extract of *Allium cepa* (AC) as a reducing agent for the optimization of its properties. The various characterization results from XRD, SEM, DRS, Raman, and VSM clearly showed that the formulated ZFNP was a single phase with crystallite size in the range of 11– 15 nm. A spherical morphology was observed for all the samples with particle size in the range of 34–52 nm. All the samples showed a superparamagnetic behavior with reduced saturation magnetization. The ZFNPs prepared were used for self-heating analysis in hyperthermia applications at 180 Oe applied field and 425 Hz. It produced enough heating within the therapeutic temperature to

This article is part of the topical collection: Nanotechnology Convergence in Africa

Guest Editors: Mamadou Diallo, Abdessattar Abdelkefi, and Bhekie Mamba

S. O. Aisida · F. I. Ezema
Department of Physics and Astronomy, University of Nigeria, Nsukka, Nigeria

S. O. Aisida · I. Ahmad
National Centre for Physics, Quaid-i-Azam University Campus, Islamabad 44000, Pakistan

S. O. Aisida · M. Maaza · F. I. Ezema
Nanosciences African Network (NANOAFNET), iThemba LABS-National Research, Somerset West, South Africa

S. O. Aisida (✉) · M. Maaza · F. I. Ezema
Nanosciences/Nanotechnology, College of Graduate Studies, University of South Africa (UNISA), Muckleneuk Ridge, P.O. Box 392, Pretoria, South Africa
e-mail: samson.aisida@unn.edu.ng

A. Ali
Center for Micro and Nano Devices, Department of Physics, COMSATS University Islamabad, Islamabad, Pakistan

O. E. Oyewande
Department of Physics, University of Ibadan, Ibadan, Nigeria

I. Ahmad · T.-k. Zhao
NPU-NCP Joint International Research Center on Advanced Nanomaterials and Defects Engineering, Northwestern Polytechnic University, Xi'an 710072, China

A. Ul-Hamid
King Fahd University of Petroleum & Minerals, Dhahran 31261, Saudi Arabia

T.-k. Zhao
School of Materials Science & Engineering, Northwestern Polytechnic University, Xi'an 710072, China

attain the Curie temperature. The ZFNP formulated is auspicious for hyperthermia applications with less side effect owing to their biocompatibility, moderate Curie temperature, and SAR value within the therapeutic range. The formulated nanoparticles have further broadened the horizon of hyperthermia therapeutic applications with an innocuous protocol within 300 s.

Highlights

- Biogenic protocol for AC-ZFNPs has been formulated in this work.
- *Allium cepa* serves as a potential reducing and stabilizing agent.
- Single-phase cubic structure and spherical nanoparticles were obtained.
- The AC-ZFNPs formed superparamagnetic nature for all the samples.
- The properties of AC-ZFNPs are highly efficient for thermoablation applications within 300 s.

Introduction

Ferrite materials have been investigated for wide biomedical applications such as magnetic storage devices (Mukherjee and Mitra 2015), targeted drug delivery (Aisida et al. 2019a), magnetic fluid (Berkovsky et al. 1993), contrast enhancement in magnetic resonance imaging (Hoque et al. 2013), hyperthermia (Sharifi et al. 2012; Hoque et al. 2016), photocatalyst in semiconductors (Jia et al. 2011), photochemical devices (Lu and Li 1992; Lv et al. 2010), tissue imaging and antibacterial agents (Aisida et al. 2019f; Aisida et al. 2019d; Aisida et al. 2019b; Aisida et al. 2019c; Madubuonu et al. 2019), and photoelectrochemical cells (McDonald and Choi 2011). All these applications are due to their properties compared to their bulk compeers (Kombaiah et al. 2017a). Among the metal ferrite nanoparticles, spinel ferrite with a general formula $X^{2+}Y_2^{3+}O_4^{2-}$, where X^{2+} signifies the divalent metal (e.g., Zn, Co) with tetrahedral cation site and Y^{3+} stands for Fe showing the octahedral cation sites while the O^{2-} shows the anion site has been distinct for these applications. Spinel ferrites are sub-divided into inverse,

normal, and mixed spinel as a result of the occupancy of the cations in interstitial sites (Brabers 1995).

Among the normal spinel ferrite, zinc ferrite nanoparticles (ZFNPs) have been used widely for various biomedical applications owing to its biocompatibility (Okoro et al. 2019). The physical properties of ferrite nanoparticles can be modified through the synthesis protocols and the surface functionalization used. Various synthesis protocols have been used to modify the general properties ZFNPs. The adopted protocol plays some viable roles in the properties of the formulated ZFNPs (Fernandes et al. 2017). The common methods often used by researchers are chemical co-precipitation (Laurent et al. 2008), microemulsion (Grasset et al. 2002), hydrothermal (Lucas et al. 2011), thermal decomposition (Okoroh et al. 2019), sol-gel (Katerina et al. 2015), and bio-based (Aisida et al. 2019a; Aisida et al. 2019f; Aisida et al. 2019d; Aisida et al. 2019b; Aisida et al. 2019c; Madubuonu et al. 2019; Aisida et al. 2019e) etcetera.

For ZFNPs to function optimally, it requires a reasonable particle size and biocompatible surface functionalization (Javed et al. 2020a; Javed et al. 2016; Ahmad et al. 2019; Javed et al. 2020b). For the formulated nanoparticles to attain its optimal functionality, a biogenic protocol with a biogenic surfactant was adopted in this work. The protocol involves the use of an aqueous extract of *Allium cepa* (AC) as a potential reducing as well as a capping agent (Nile and Park 2013; Heikal et al. 2020). This is due to the inherent phytochemicals (PTC) bloated in AC. *Allium cepa* has been widely used as a flavoring vegetable owing to its intrinsically rich in PTC, such as flavonoid (with about 16 types, particularly quercetin), resin, alkaloid, and terpenes. All these enhanced its bioactive potency (Nile and Park 2013).

Thermoablation via nanotherapy is a propitious biomedical application of magnetic nanoparticles chiefly for cancer therapy (Giustini et al. 2010; Shete et al. 2014). This method is highly preferable owing to its double operation as thermal ablation against cancerous cells within the therapeutic ambit (40–45 °C) and also as an adjuvant with other potent therapies like chemotherapy and radiation therapy to enhance their potency at the targeted site (Van et al. 2004). The rationale behind magnetic nanoparticle (MNP)–based thermoablation for nanotherapy involves the use of magnetic nanomaterials under the influence of an alternating magnetic field (AFM) and the heterogeneous nature of tumor tissues (Otte 1988). The enhancement of thermoablation for nanotherapy is broadly dependent on the alternative magnetic field (AMF)

amplitude, the magnetic properties, the frequency, the shape, and the size of the particles (Zhang et al. 2008).

In this work, we have prepared ZFNPs functionalized with various concentrations of AC (20%, 40 % and 60%) by the biogenic method to enhance its bio-compatibility. This method uses cost-effective, eco-friendly, and innocuous AC as a potential reducing agent to enhance the stability of the formulated colloidal solution for the first time. To our knowledge, the evaluation of the effects of AC on the properties of ZFNPs and its thermoablation evaluation has not been reported in the literature. Hence, the microstructural properties of the colloidal AC-ZFNPs were affirmed by SEM, TEM, and XRD. The optical properties were evaluated by UV-Vis DRS and Raman spectral analyses; the magnetic properties were analyzed by VSM. The properties of ZFNPs were greatly enhanced by the concentration of AC. Also, the highest temperature and the specific absorption rate (SAR) for thermoablation were influenced by the concentration of AC. It is noteworthy that the influence of AC reduces the heating rate from 49 to 34 within 300 s to obtain the highest temperature within the therapeutic range. Hence, the properties of AC-ZnFNPs obtained are auspicious for thermoablation applications.

Materials and experimentation

Materials

Sigma-Aldrich products of zinc nitrate hexahydrate $(Zn(NO_3)_2 \cdot 6H_2O)$ and iron (III) nitrate nonahydrate $(Fe(NO_3)_3 \cdot 9H_2O)$ precursors were procured commercially in Pakistan in their analytical grade. *Allium cepa* (AC) was obtained from a local market and used as a potential reducing agent. Distilled water (DW) was used for all solution preparations and washing of the glassware.

Allium cepa preparation

The obtained *Allium cepa* bulb was washed with DW twice to enhance its neatness. The first two layers were exfoliated and the bulb is cut into small pieces using a sterilized knife. Ten-gram portion of the pieces were liquefied in 100 mL DW and boil for 80 °C under magnetic stirrer at 500 rpm for 1 h followed by filtration using a fine pore sieve and mill pore filter paper. The obtained solvent was stored in a refrigerator at 4 °C for biosynthesis.

AC-ZFNP biogenic preparation

The nominal compositions of ZFNPs and AC-ZFNPs (20%, 40 % and 60%) have been formulated using the biogenic method. The stoichiometric ratio of the precursors was dispersed in 100 mL of DW and stirred at 800 rpm for 1 h to attain a homogeneous solution. Unto the homogeneous sol formed, 20% aqueous extract of AC was added dropwise under 800 rpm constant stirring at 70 °C for 2 h to form a brown gel. A color change was gradually observed after the introduction of AC. This is an indication of the formulation of AC-ZFNPs colloid. The formulated gel was transferred into the muffle furnace oven to complete the drying at 70 °C for 6 h. The obtained nanoparticles were collected and pulverized with agate mortar and pestle to form fine powders followed by calcination at 900 °C for 3 h in a hot air vacuum tube furnace. These procedures were repeated stepwise for the preparation of other samples with 40% and 60% AC. The formulated ZFNPs and AC-ZFNPs were characterized using different techniques.

PTC analysis

The PTC analysis of total flavonoid properties (TFP) and total alkaloid properties (TAP) inherent in AC was assessed following the previous procedures by Javed et al. (Javed et al. 2017), with little modifications. The TAP was determined using Folin-Ciocalteu reagent. Twenty microliters from 4 mg/mL of the formulated sample was homogenized in 90 µL of Folin-Ciocalteu and then incubated at room temperature for 5 min for good diffusion. After incubation, 90 µL of Na_2CO_3 was introduced into the solution, followed by 80-min incubation at room temperature to neutralize the reaction. The procedures were run in triplicate using gallic acid as a control. The absorbance was read at 630 nm and TAP was quantified as µg equivalent of gallic acid. The TFP was analyzed using the aluminum chloride colorimetric method. Two hundred fifty microliters of the test sample in the mixture was dispersed in 75 µL $NaNO_2$ (5%w/v) solution in a test tube, 10 µL of 10% aluminum chloride and potassium acetate (1.0 M). The solution was made of with distilled water followed by incubation at room temperature for 30 min. Quercetin (QE) was used as the control and the absorbance was recorded at 630 nm. The obtained results were expressed as Quercetin equivalent in µgQE/mg.

Cytotoxicity assay of AC-ZFNPs

The in vitro toxicity test of AC-ZFNPs was determined following the procedures of Andrej et al. (Andrej et al. 2014), with some modifications. The hemolytic assay was performed using the following chemicals: Triton X-100, phosphate buffer saline (PBS), and EDTA. Fifty microliters DMSO serves as the negative control, while 0.5% triton X-100 serves as the positive control. Human erythrocytes were obtained from fresh human blood and 1 mL of blood was centrifuged for 5 min at 14,000 rpm to obtain erythrocytes. To the clean erythrocyte solution, phosphate buffer saline (PBS) was added in ratio 1:1 in a tube and centrifuged at 2000 rpm for 10 min to wash the solution. The process was repeated three times. Pellet of 200 μL was removed after the last wash in a falcon tube containing 4800 μL of PBS to prepare 4% erythrocyte cell suspension according to the requirement of the samples and was ready for further use. After that, the formulated nanoparticles with different concentrations, i.e., 20 μL, 15 μL, 10 μL, and 5 μL from 4 mg/mL, were placed in Eppendorf tubes by addition of 180 μL, 185 μL, 190 μL, and 195 μL to make the final concentration of 200 μL and incubated for 1 h at 37 °C. The tubes were centrifuged for 10 min at 2500 rpm from which 100 μL of the supernatant was transferred to 96-well plates. The absorbance of the solution was taken at 540-nm wavelength on the microplate reader (ELx 800 BioTek). The optical density (OD) of the formulated AC-ZFNP positive and negative control samples were evaluated at 540 nm (Manjul and Geeta n.d.; Kapusetti et al. 2012). The generally acceptable tolerable limit of hemolysis for biomedical applications must be ≤5% (Autian 1975).

Characterization techniques of AC-ZFNPs

The phase analysis of AC-ZFNPs was determined using powder X-ray diffraction (XRD) spectroscopy, a Shimadzu LabX 6100 diffractometer using Cu-kα radiation with a wavelength of 1.5418 Å. The thermogravimetric analysis (TGA) was performed using the DTG-60H (Shimadzu) thermal analyzer in the temperature range of 49–995 °C at the heating rate of 20 °C per min. Under nitrogen atmosphere. The optical properties of the samples were determined using Uv-visible diffuse reflectance spectra (Uv-DRS) Cary100 Uv-visible spectrophotometer. Scanning electron microscopy (SEM) and transmission electron microscopy (TEM) were used to determine the morphological analyses of the samples.

Raman analyses were conducted with the DV420_OE model at a frequency of 1470 Hz. The magnetic properties were conducted using a vibrating sample magnetometer (VSM) Quantum design Versa lab Measurement system with a superconducting magnet and the applied field in the range of ±20 KOe. The heating ability was conducted using an alternating magnetic field (AMF) of amplitudes 180 Oe at a frequency of 425 kHz (COMDEL CLF-5000, USA RF generator).

Results and discussion

Structural analyses of ZFNPs and AC-ZFNPs

The structural analyses of ZFNPs and AC-ZFNPs were determined using powder X-ray diffraction spectroscopy (as shown in Fig. 1). The various diffraction peak intensities become sharper and devoid of impurities as the concentration of AC increases showing the polycrystalline characteristics cubic structure. The obtained 2θ values and their corresponding crystallographic planes of 18.2° (111), 29.9° (220), 35.2° (311), 36.8° (222), 42.8° (400), 53.1° (422), 56.6° (511), 62.1° (440), 70.5° (620), 73.5° (533), 74.5° (622), and 78.4° (444) are well indexed with the JCPD file no. 89–4926 (Yang et al. 2013). The crystallite size (D) as presented in Table 1 was determined using the Debye-Scherer's equation (Eq. 1) for all the planes with a value of 33.4, 40.6, 46.6, and 54.4 nm for a, b, c, and d samples, respectively. The value of D shows the nanosize range of the colloidal samples. This is observed to be consistent with the particle size obtained by SEM analyses. The AC concentration influenced the colloidal formation by increasing the crystallite size (as shown in Fig. 2a). Also, the microstrain ( ) of the formulated AC-ZFNPs (Mocherla et al. 2014) was evaluated using Eq. 2. From the XRD (311) plane broadening, the microstrain was found to decrease as the crystallite size increases. The observed systematic decrease in the microstrain with a corresponding decrease in 2θ values shows strain-induced structural changes in AC-ZFNPs as the AC concentration increases (as shown in Fig. 2d).

$$D = \frac{0.9}{\Re \, \mathrm{Cos}\theta} \cdot \lambda \qquad (1)$$

$$\mho = \frac{\Re \, \mathrm{Cos}\theta}{4} \qquad (2)$$

Fig. 1 XRD spectra analyses of (**a**) ZFNPs and (**b–d**) AC-ZFNPs at 20%, 40%, and 60% AC
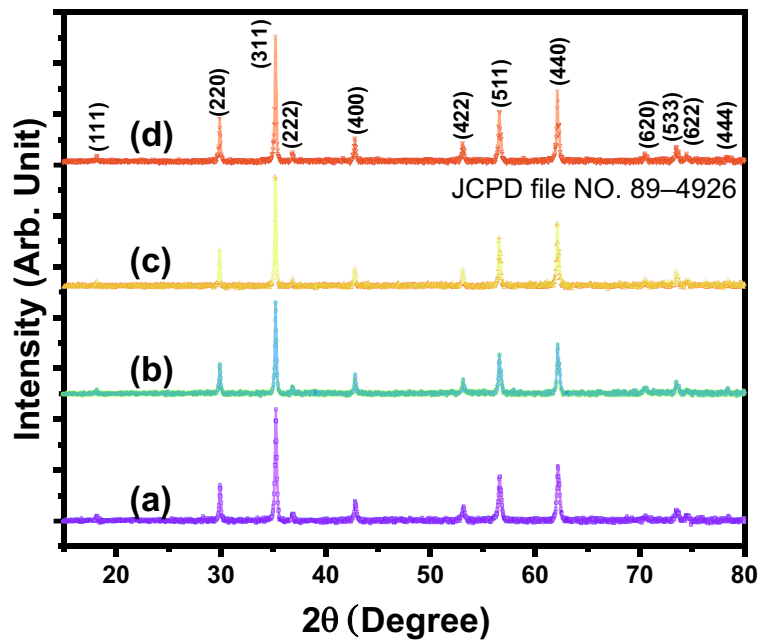
where D is the average crystallite size (nm), λ is the X-ray wavelength ($\lambda = 0.15406$ nm), $\Re$ is the full width at half maximum (FWHM) intensity measured in radians, is the microstrain, and θ is the Bragg diffraction angle of the plane (Cullity 1978).

Morphological analyses of ZFNPs and AC-ZFNPs

A SEM micrograph was used to analyze the morphology of ZFNPs and AC-ZFNPs formulated. The SEM micrograph, as presented in Fig. 3, shows spherical morphology for all the samples. The corresponding particle size distribution histogram analyzed by ImageJ software, as presented in Fig. 3a–d inset, gives an average particle size in the range of 12–30 nm. The particle size is AC concentration-dependent (as shown in Table 1). This may be adduced to the ionic distribution of AC in the

samples, which enhances the growth rates of the formulated crystals. The decrease in particle size has been observed to invariably lead to a decrease in the surface to volume ratio of the obtained nanoparticles. The obtained morphologies were further examined with transmission electron microscopy (TEM). Figure 3 e and the magnification in the inset showed the spherical nature of the formulated ZFNPs. The elemental composition determined by SAED, as shown in Fig. 3f, confirmed the crystalline nature of the sample. The observed rings were attributed to the diffraction plane from (220), (311), (400), (422), (511), and (440), respectively. The EDX analysis of the formulated nanoparticles, as shown in Fig. 3g, gives an evidence of the sample's purity and the presence of the constituent elements almost in their stoichiometry ratio for all the concentrations with Fe and Zn showing the strongest

Table 1 The crystallite size, particle size, and bandgap of ZFNPs and AC-ZFNPs

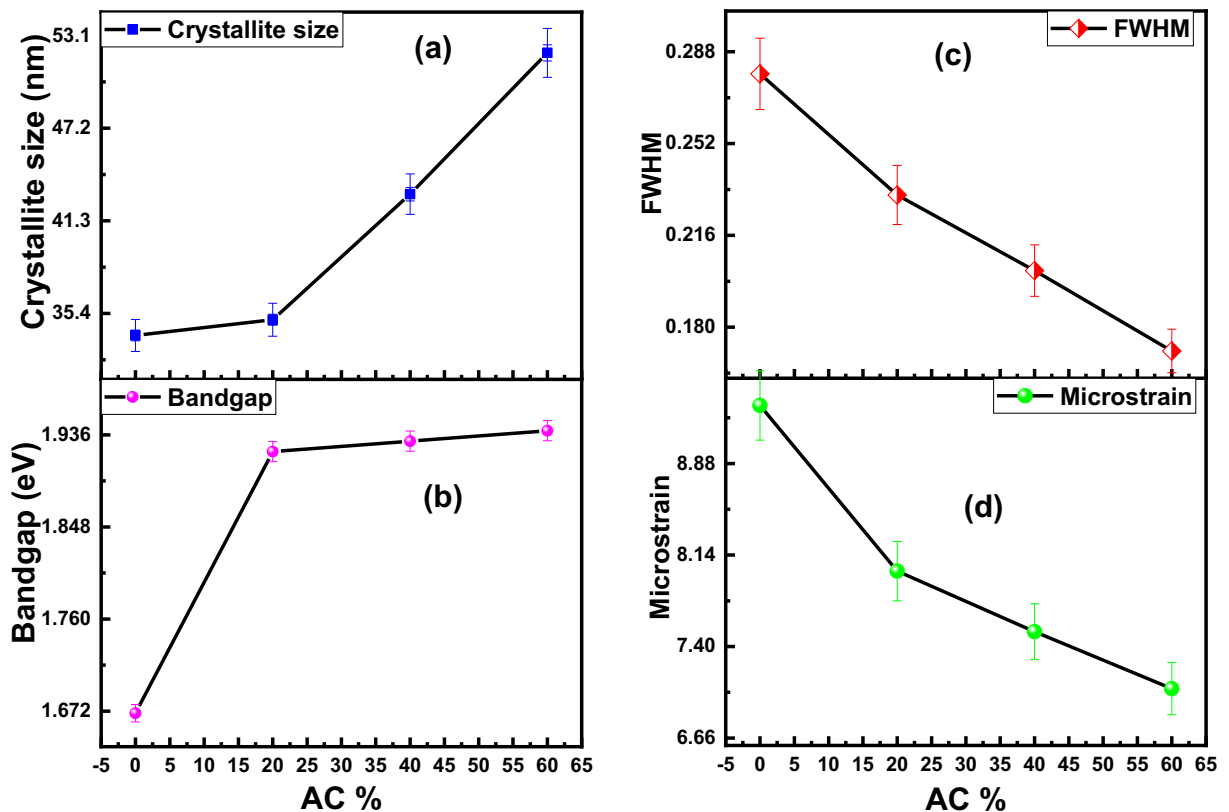| Sample	FWHM ($\Re$)	2θ (°)	D (nm)	Xc (nm)	E_g (eV)	(10^{-4})
ZFNPs	0.279354	35.3	33.4	34 ± 12.9	1.67	9.3
ZFNPs+20% AC	0.231848	35.3	40.6	35 ± 17.3	1.92	8.0
ZFNPs+40% AC	0.202198	35.3	46.6	43 ± 29.9	1.93	7.5
ZFNPs+60% AC	0.17068	35.3	54.4	52 ± 30.4	1.94	7.0

Fig. 2 (a) Particle size, (b) bandgap and particle size, and (c) FWHM and (d) microstrain against AC%

peaks at 6.4 keV and 1.2 keV respectively along with other minor elements N and O.

Optical properties of ZFNPs and AC-ZFNPs

Uv-visible diffused reflectance spectroscopy (DRS) was used to analyze the optical properties of ZFNPs and AC-ZFNPs as presented in Fig. 4(i). The inset in Fig. 4(i) shows the color change during absorption between the oxidizing and reducing agents for the formulation of AC-ZFNPs. The bandgap of the samples, as presented in Table 1, was determined by converting the reflectance using the Kubelka-Munk (KM) relation theory and Tauc plot as shown in Eq. 3.

$$F(R) = \frac{\mu}{s} = \frac{(1-R)^2}{2R} \tag{3}$$

The energy bandgap for the direct transition ($n = 2$) using the Tauc plot (Eq. 4) as shown in Fig. 4(ii) of the

samples is obtained via extrapolating the slope $[F(R).h\upsilon]^n \approx 0$.

$$(\mu h v)^2 = A(hv - E_g) \tag{4}$$

The bandgaps of the samples are obtained by $(\mu h v)^2$ vs. hv plot from the Tauc's relation (Eq. 4) (Khan et al. 2013; Sagar et al. 2012). It is obvious that the bandgap is AC concentration-dependent (as shown in Fig. 2a). Studies showed that the energy bandgap of nanoparticle materials is majorly influenced by impurities from surfactants, calcination effect, method of preparation, and the crystallite size (Tatarchuk et al. 2018; Beltran et al. 2015). The increase in the energy band gap is in agreement with the state-of-the-art report (Sagar et al. 2012).

Raman analyses of ZFNPs and AC-ZFNPs

The Raman spectra analysis of ZFNPs and AC-ZFNPs presented in Fig. 5 are within the range of 200–1500 cm^{-1}. The optical phonon distribution in Raman spectra as predicted by group theory analyses is given by 5T1u + A1g + Eg + 3T2g, where the 5T1u modes are
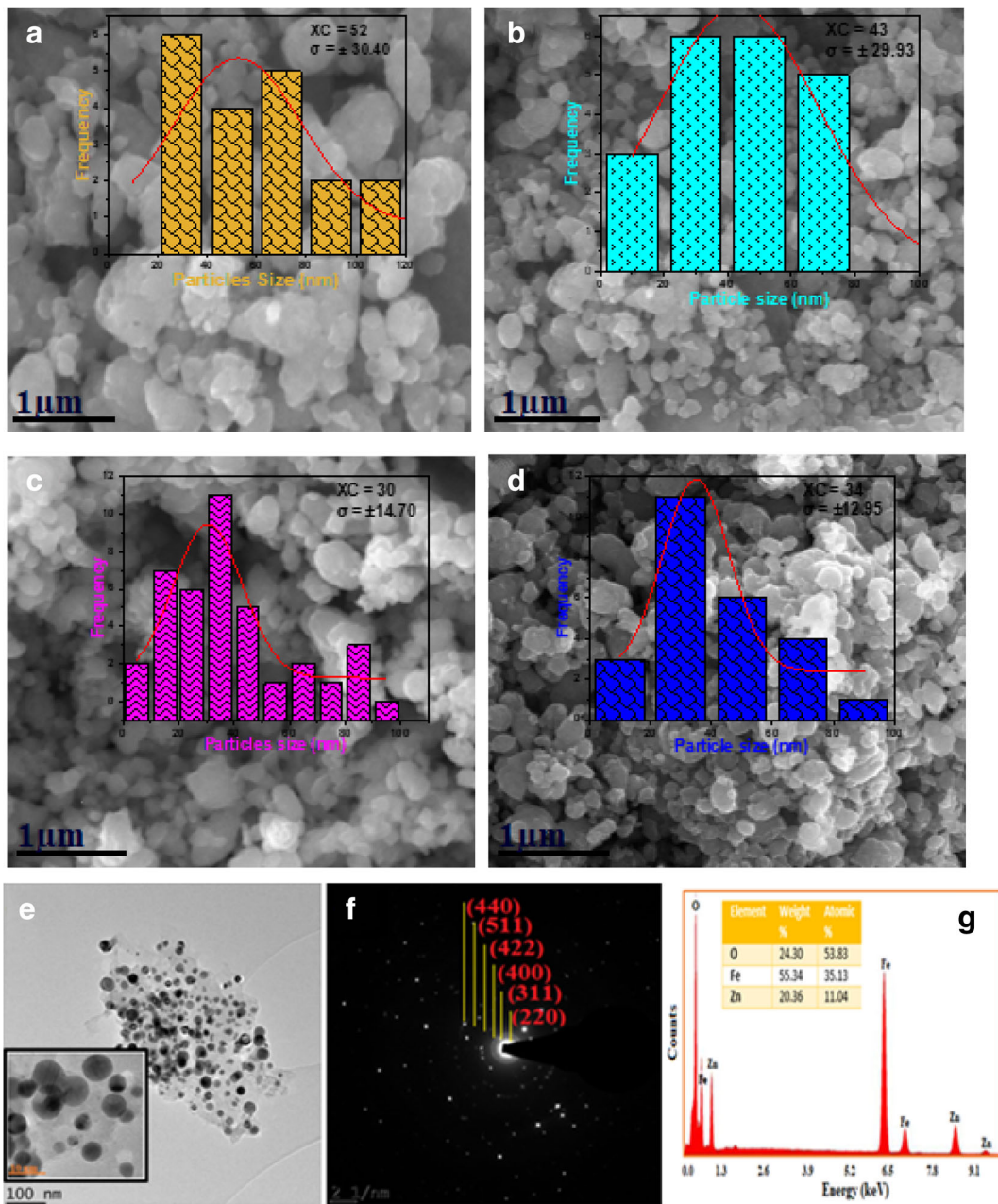
Fig. 3 SEM micrograph and particle size distribution analyses of **a** ZFNPs and AC-ZFNPs at **b** 20%, **c** 40%, and **d** 60% AC. **e** TEM micrograph analysis of AC-ZFNPs for 60% AC **f** SAED and **g** EDX

infrared (IR) active while (A1g + Eg + 3T2g) modes are Raman active modes assigned to the A-site, B-site, and O ions in the $ZnFe_2O_4$ spinel structures (Chandramohan et al. 2011). From the formulated samples, four major spectra were observed. The spectra around 230–240, 290–360, 430–360, and 590–710 cm^{-1} ranges are assigned to the T2g (3), E_g, T2g (2), and A1g modes,

respectively. The T2g modes are as a result of the asymmetric stretching of the oxygen anion in line to the tetrahedral and octahedral cations, while the A1g and Eg modes are ascribed to the symmetric stretching and bending of the oxygen anions, respectively (Yu et al. 2002). The mode at A1g is ascribed to the stretching vibration of Fe-O and X-O (divalent metals)
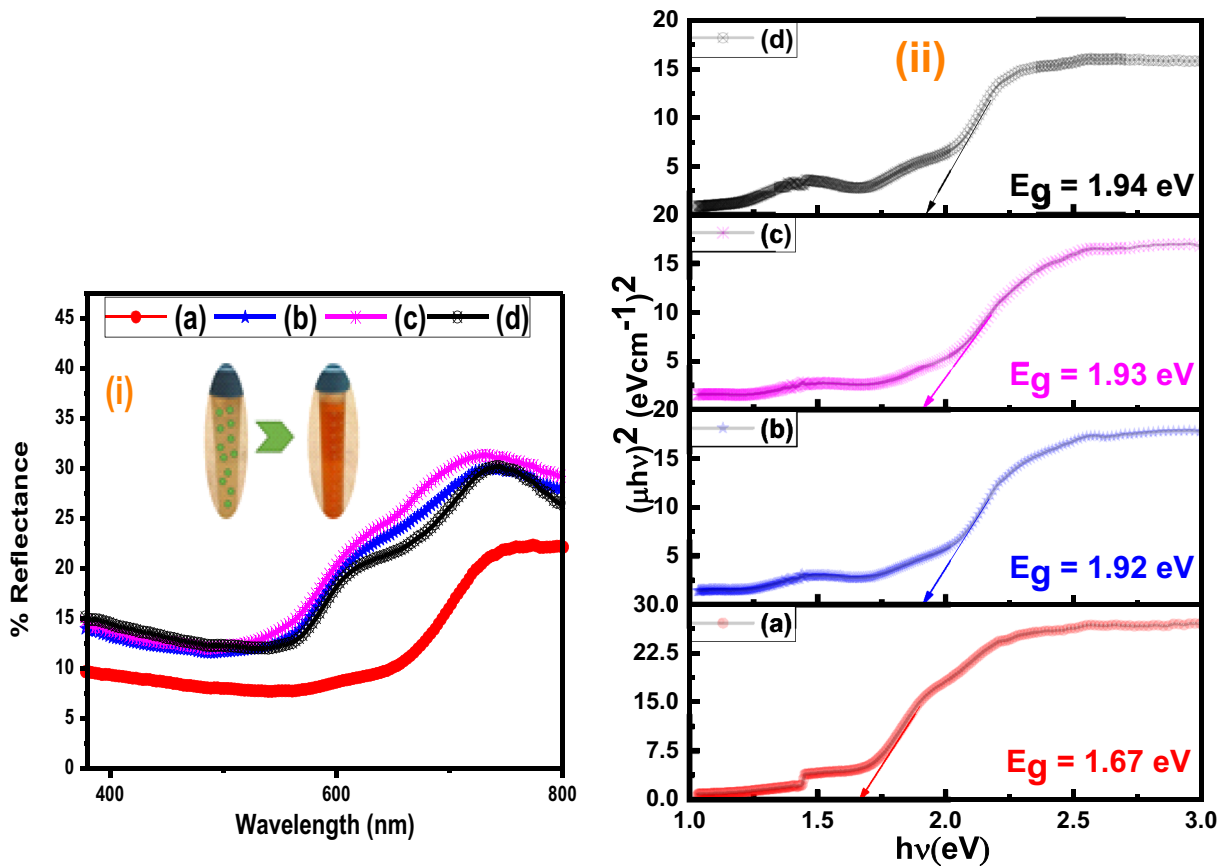
Fig. 4 (i) UV-DRS reflectance spectra, the inset shows the color change for the formulation of AC-ZFNP (ii) bandgap of (a) ZFNPs and (b–d) AC-ZFNPs at 20%, 40%, and 60% AC, respectively

in the tetrahedral sites. The other lower Raman modes are assigned to T2g (2), E_g, and T2g (3) modes showing the vibration of the spinel structure (Chandramohan et al. 2011; Yu et al. 2002). The intensity of the vibration modes slightly shifted to the lower wavelength as the concentration of AC increases. This is also observed by Raghvendra et al., using honey-mediated Co Fe_2O_4 annealed at a different temperature (Raghvendra et al. 2017).

Magnetic properties of ZFNPs and AC-ZFNPs

The magnetization (M) versus the magnetic field (H) of ZFNPs and AC-ZFNPs conducted at T_R by VSM are presented in Fig. 6(i). The hysteresis loop shows the magnetic properties of the samples under the influence of AC concentration. The inset in Fig. 6(i) shows the magnification of the M-H loop for easy identification of the properties. All the samples exhibited superparamagnetism, i.e., the

formation of (M-H) loop in which the magnetization passes through the origin. As the AC % increases, the saturation magnetization (M_s) increases respectively with approximately zero coercivity (H_c), that is, the measure of the applied field in the reverse direction assigned to force the remanent magnetization (M_r) back to zero (as presented in Table 2 and Fig. 6(ii)). The decrease in M_s is owing to the cation site distribution in the spinel ferrite structure caused by AC, which is in agreement with the previous results recorded by Unchista et al., on Co1−xNixFe2O4 using *Aloe vera* extract (Unchista et al. 2016).

The Bohr magneton (n_B) of the magnetic moment and the anisotropy constant (K) were obtained using Eqs. 5 and 6, respectively (Nikam et al. 2015; Kambale et al. 2009). The influence of AC concentration curiously changed the value K of the formulated samples as observed from the H_c values (as presented in Table 2).

Fig. 5 Raman spectra analyses of (**a**) ZFNPs and (**b–d**) AC-ZFNPs at 20%, 40%, and 60% AC
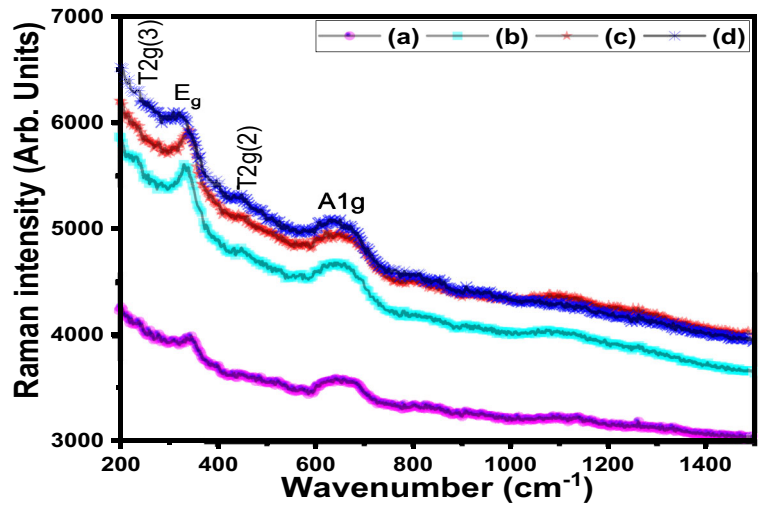
$$n_B = \frac{M_W \times M_s \times 10^{-3}}{N_A \times \mu_B} \qquad (5)$$

$$K = \frac{H_c \times M_s}{0.96} \qquad (6)$$

where n_B, M_W, M_s, N_A, μ_B, K, and H_c are the magnetic moment in Bohr magneton, the molecular weight of the precursor (mole/g), saturation magnetization, Avogadro's number ($N_A = 6.02 \times 10^{23}$ mol^{-1}), the magnetic moment of electron ($\mu_B = 9.27 \times 10^{-24} Am^2$), anisotropy constant, and coercivity, respectively. The decrease in M_s, K, and n_B, as shown in Table 2, may be adduced to the concentration of AC in the composited samples. The observed decrease in M_s was due to the substitution of AC in the sample, which indirectly alters the magnetic moment. This is because the distribution of cation inversion among the A-B interstitial
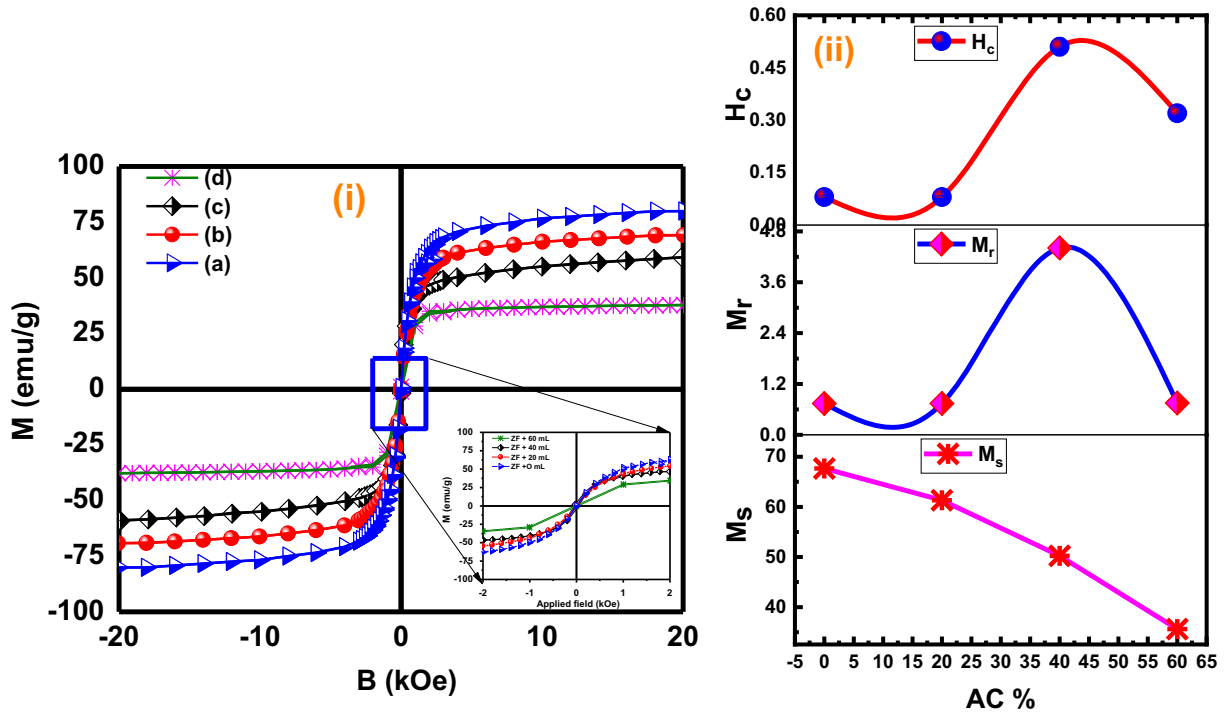

Fig. 6 (i) Hysteresis of (**a**) ZFNPs and (**b–d**) AC-ZFNPs at 20%, 40%, and 60% AC. (ii) M_s, M_r, and H_c against AC

Table 2 Parameters of the magnetic properties and SAR values of ZFNPs and AC-ZFNPs

Sample	M_s (emu/g)	M_r (emu/g)	H_c (Oe)	M_r/M_s	n_B (μ_B)	K (erg/g)	Mass conc. (mg/mL)	Initial slope ($^\theta$C/s)	SAR (W/g)
ZF+0%	67.67	0.74	0.08	0.012	3.72	5.64	17	1.0618	39.74
ZF+20%	61.32	0.74	0.08	0.012	3.38	5.11	17	0.8725	32.60
ZF+40%	50.23	4.41	0.51	0.495	2.77	26.7	17	0.7000	26.24
ZF+60%	35.63	0.75	0.32	0.476	1.97	11.9	17	0.5060	18.96

sites is stronger than A-A and B-B interactions, according to the Neel model (Patrick 1988). The anisotropy equation (Eq. 5) is effective for non-interacting particles with uniaxial anisotropy in their random distribution. The remanence ratio of M_r/M_s is a special parameter that defines the characteristic of magnetic materials with information about the reorientation of the magnetic directions to the nearby axis after the removal of the magnetic field (Gore et al. 2015). The M_r/M_s

of our samples is between 0.012 and 0.476; these values signifying uniaxial anisotropy dominated behavior of the formulated samples compared to ≈ 0.83 expected value for cubic anisotropy exhibited by bulk zinc ferrite (Bedanta and Kleemann 2009; Muscas et al. 2015). The value of D also plays some momentous role in the decrease of M_s after the addition of AC compared to the bulk value 93.9 emu/g reason attributed to the surface defect and the cation distribution (Kombaiah et al. 2017a).

Self-heating analyses of ZFNPs and AC-ZFNPs

Self-heating analyses of ZFNPs and AC-ZFNPs dispersed in de-ionized water have been recorded using Magnetherm Nanotherics (MN) with an alternating magnetic field (AMF) of 180 Oe at a frequency of 425 kHz for all the samples as shown in Fig. 7a. Seventeen milligrams of each concentration of the formulated nanoparticles was dispersed in 1 mL of DW and sonicated for 10 min and the temperature (T) against time (t) was recorded using Eq. 7. The self-heating of the formulated samples was evaluated using the specific absorbance rate (SAR) analyses (as described in Eq. 8).

$$T = \Delta T + RT \tag{7}$$

$$SAR\ (AC{-}ZFNPs) = C \cdot \frac{\Delta T}{\Delta t} \cdot \frac{M_s}{M_w} \tag{8}$$

where RT is the room temperature, ≈ 20 °C, C is the specific heat capacity of the sample, M_s is the mass of the sample, M_w, the total mass of the compound, and $\frac{\Delta T}{\Delta t}$ (heating rate).

The self-ablation at room temperature (≈ 20 °C) of the formulated samples, as shown in Fig. 7a, gives a sharp curve of increase in temperature with time to attain the highest temperature for the therapeutic range (40–48 °C) (Monrudee et al. 2011). The heating rate decreases as the percentage concentration of AC increases
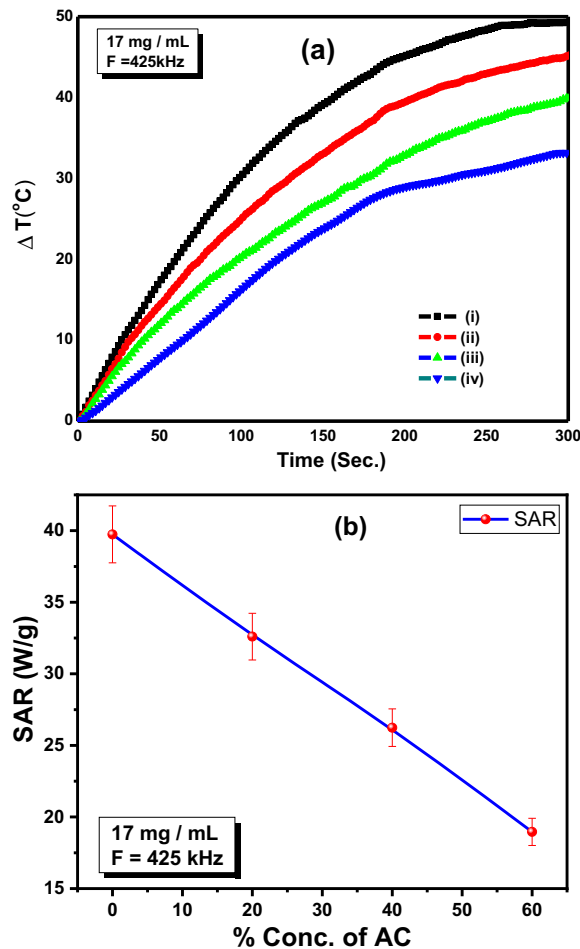

Fig. 7 a Heating analysis of (i) ZFNPs and (ii–iv) AC-ZFNPs at 20% 40% and 60% AC. **b** SAR against AC

to attain the therapeutic range (as observed in Fig. 7a). Hence, the ZF formulated at 60% of AC falls within the therapeutic range. Study shows that parameters like a magnetic field and the frequency also define the heating temperature of hyperthermia (Appa et al. 2019). The sharp curve observed in the formulated samples is synonymous with the results of other researchers with ferrite materials. The heat losses are owing basically to Brownian (single domain) and Neel/Brownian (multidomain) (Dong-Hyun et al. 2008; Deatsch and Evans 2014). The efficiency of the tumoricidal of the formulated nanoparticles was further studied through the specific absorption rate (SAR) evaluated using Eq. 8 which determines the amount of heat generated by the MNPs with respect to the AC concentration as shown in Fig. 7b. The SAR value decreases as the concentration of AC increases as presented in Fig. 7b and Table 2. The maximum temperature value with the SAR also decreases and are all within the range of 38–48 °C. The sample with 60% AC has proved to be more effective and most appropriate for hyperthermia treatment with 10.96 W/g SAR value and high-temperature rate within 300 s.

The SAR value of the formulated samples is in agreement and better at 60% AC than Kombaiah et al. result of 14.63 with $CuFe_2O_4$ at 331 kHz and 17 mT prepared by conventional combustion method (Kombaiah et al. 2017b). Studies showed that the SAR values obtained by different researchers depend on a different parameter such as measurement of SAR, sample volume, the frequency used, the applied magnetic field, and also, the shape of the container.

Conclusion

Biogenic synthesis protocol for ZFNPs and AC-ZFNPs has been successfully obtained using AC as a biological reducing and capping agent for moderate hypertermia property optimization. The XRD analysis of the formulated samples exhibited cubic phase structure. The TEM results showed spherical particles of the samples with an average particle size in the range of 34–52 nm. The optical properties through the DRS analysis gave the energy bandgap between 1.67 and 1.94 eV. The obtained energy bandgap increased with the concentration of AC. Also, the Raman analysis revealed the optical phonon distribution with Raman mode in the range of 200–800 cm^{-1}. The VSM analysis revealed the

superparamagnetic nature of the samples with a decrease in the M_s as the % AC concentration increases. The self-heating of the formulated samples generate enough heating within the therapeutic temperature range 33–49 °C within 300 s to attain the highest temperature. This makes it a better candidate for magnetic hyperthermia applications. An increase in the concentration of AC atom reduces the heating temperature from 49 to 33 °C, to fall within the therapeutic range. Optimized properties of the formulated samples were obtained by the AC concentrations which are propitious for hyperthermia application with moderate SAR values within the therapeutic range. The obtained sample is projected for further in vivo and in vitro application in the future with thorough cytotoxicity assay.

Declarations

Conflict of interest   The authors declare no competing interests.

References

Ahmad M, Yuesuo Y, Ao Q, Adeel M, Hui Z, Rabia J (2019) Appraisal of comparative therapeutic potential of undoped and nitrogen-doped titanium dioxide nanoparticles. Molecules 24:3916

Aisida SO, Akpa PA, Ahmad I, Zhao T, Maaza M, Ezema FI (2019a) Bio-inspired encapsulation and functionalization of iron oxide nanoparticles for biomedical applications. Eur Polym J 122:109371

Aisida SO, Madubuonu N, Alnasir MH, Ahmad I, Botha S, Maaza M, Ezema FI (2019b) Biogenic synthesis of iron oxide nanorods using Moringa oleifera leaf extract for antibacterial applications. Appl Nanosci 10:305–315

Aisida SO, Ugwoke E, Uwais A, Iroegbu C, Botha S, Ahmad I, Maaza M, Ezema FI (2019c) Incubation period induced biogenic synthesis of PEG enhanced Moringa oleifera silver nanocapsules and its antibacterial activity. J Polym Res 26: 225

Aisida SO, Ugwu K, Akpa PA, Nwanya AC, Nwankwo U, Botha SS, Ejikeme PM, Ahmad I, Maaza M, Ezema FI (2019d) Biosynthesis of silver nanoparticles using bitter leave

(Veronica amygdalina) for antibacterial activities. Surf Interface 17:100359

Aisida SO, Akpa PA, Ahmad I, Maaza M, Ezema FI (2019e) Influence of PVA, PVP and PEG doping on the optical, structural, morphological and magnetic properties of zinc ferrite nanoparticles produced by thermal method. Phys B Condens Matter 571:130–136

Aisida SO, Ugwu K, Akpa PA, Nwanya AC, Ejikeme PM, Botha SS, Ahmad I, Maaza M, Ezema FI (2019f) Biogenic synthesis and antibacterial activity of controlled silver nanoparticles using an extract of Gongronema latifolium. Mater Chem Phys 237:121859

Andrej O, Rena'ta O, Zuzana OK, Andrea MT, Kupkova M, Monika H, Jozef R, Ro'bert D (2014) Sintered metallic foams for biodegradable bone replacement materials. J Porous Mater 21:131–140

Appa PR, Srinivasa KR, Pydi TR, Govinda K, Mounika C, Chaitanya MV, Rao K (2019) A systematic study of cobalt-zinc ferrite nanoparticles for self regulated magnetic hyperthermia. J Alloys Compd 794:60–67

Autian J (1975) Polymer science and technology. Polym Med Surg 8:181–203

Bedanta S, Kleemann W (2009) Supermagnetism. J Phys D Appl Phys 42:013001

Beltran JJ, Barrero CA, Punnoose A (2015) Understanding the role of iron in the magnetism of Fe doped ZnO nanoparticles. Phys Chem Chem Phys 17:15284e15296

Berkovsky BM, Medvedev VF, Krakov MS (1993) Magnetic fluids: engineering applications, first edn. Oxford University Press, Oxford

Brabers V (1995) Progress in spinel ferrite research. Handb Magn Mater 8:189–324

Chandramohan P, Srinivasan M, Velmurugan S, Narasimhan S (2011) Cation distribution and particle size effect on Raman spectrum of CoFe2O4. J Solid State Chem 184:89–96

Cullity B (1978) Element of X-ray diffraction, 2nd edn. Addison-Wesley, London, p 102

Deatsch EA, Evans BA (2014) Heating efficiency in magnetic nanoparticle hyperthermia. J Magn Magn Mater 354:163–172

Dong-Hyun K, David EN, Duane TJ, Christopher SB (2008) Heat generation of aqueously dispersed CoFe2O4 nanoparticles as heating agents for magnetically activated drug delivery and hyperthermia. J Magn Magn Mater 320:2390–2396

Fernandes I d M, Lopes-Moriyama AL, de Souza CP (2017) Effect of synthesis parameters on the size of cobalt ferrite crystallite. Ceram Int 43:3962–3969

Giustini AJ, Alicia AP, Shiraz MC, Jennifer AT, Ian B, Jack HP (2010) Magnetic nanoparticle hyperthermia in cancer treatment. Nano Life 01:17–32

Gore S, Mane R, Naushad M, Jadhav S, Zate M, Alothman Z, Hui B (2015) Influence of Bi3+-doping on the magnetic and Mössbauer properties of spinel cobalt ferrite. Dalton Trans 44:6384–6390

Grasset F, Labhsetwar N, Li D, Park D, Saito N, Haneda H, Cador O, Roisnel T, Mornet S, Duguet E, Portier J, Etourneau J (2002) Langmuir 18:8209

Heikal YM, AncaȘuțan N, Rizwan M, Elsayed A (2020) Green synthesized silver nanoparticles induced cytogenotoxic and genotoxic changes in Allium cepa L. varies with nanoparticles doses and duration of exposure. Chemosphere 243:125430

Hoque S, Srivastava C, Venkatesha N, Kumar P, Chattopadhyay K (2013) Superparamagnetic behaviour and T1, T2 relaxivity of ZnFe2O4 nanoparticles for magnetic resonance imaging. Philos Mag 93:1771–1783

Hoque SM, Hossain MS, Choudhury S, Akhter S, Hyder F (2016) Synthesis and characterization of ZnFe2O4 nanoparticles and its biomedical applications. Mater Lett 162:60–63

Javed R, Usman M, Tabassum S, Zia M (2016) Effect of capping agents: structural, optical and biological properties of ZnO nanoparticles. Appl Surf Sci 386:19–26

Javed R, Ahmed M, Haq I u, Nisa S, Zia M (2017) PVP and PEG doped CuO nanoparticles are more biologically active: antibacterial, antioxidant, antidiabetic and cytotoxic perspective. Mater Sci Eng C Mater Biol Appl 79:108–115

Javed R, Rais F, Fatima H, Ihsan U, Muhammad K, Sohaila SN, Ao Q (2020a) Chitosan encapsulated ZnO nanocomposites: fabrication, characterization, and functionalization of bio-dental approaches. Mater Sci Eng C 116:111184

Javed R, Zia M, Naz S, Aisida S, Ain N, Ao Q (2020b) Role of capping agents in the application of nanoparticles in biomedicine and environmental remediation: recent trends and future prospects. J Nanobiotechnol 18:172

Jia Z, Ren D, Liang Y, Zhu R (2011) A new strategy for the preparation of porous zinc ferrite nanorods with subsequently light-driven photocatalytic activity. Mater Lett 65:3116–3119

Kambale R, Shaikh P, Kamble S, Kolekar Y (2009) Effect of cobalt substitution on structural, magnetic and electric properties of nickel ferrite. J Alloys Compd 478:599–603

Kapusetti G, Misra N, Singh V, Kushwaha RK, Mati P (2012) Bone cement/layered double hydroxidenanocomposites as potential biomaterials for joint implant. J Biomed Mater Res A 100:3363–3373

Katerina Z, Vicente R, Martin T, Zara C-Z, Boris K, Raquel T, Ivan M, Maria M (2015) Preparation, characterization and application of nanosized copper ferrite photocatalysts for dye degradation under UV irradiation. Mater Chem Phys 160: 271–278

Khan JA, Qasim M, Singh BR, Singh S, Shoeb M, Khan W, Das D, Naqvi AH (2013) Synthesis and characterization of structural, optical, thermal and dielectric properties of polyaniline/CoFe2O4 nanocomposites with special reference to photocatalytic activity. Spectrochim Acta A Mol Biomol Spectrosc 109:313–321

Kombaiah K, Judith JV, John LK, Bououdina M, Hamad AA-L, Jothi RR (2017a) Studies on Opuntia dilenii haw mediated multifunctional ZnFe2O4 nanoparticles: optical, magnetic and catalytic. Mater Chem Phys 194:153–164

Kombaiah K, Vijaya JJ, Kennedy LJ, Bououdina M, Al-Najar B (2017b) Conventional and microwave combustion synthesis of optomagnetic CuFe2O4 nanoparticles for hyperthermia studies. J Phys Chem Solids 115:162–171

Laurent S, Forge D, Port M, Roch A, Robic C, Vander EL, Muller R (2008) Magnetic iron oxide nanoparticles: synthesis, stabilization, vectorization, physicochemical characterizations, and biological applications. Chem Rev 108:2064–2021

Lu G, Li S (1992) Hydrogen production by H2S photodecomposition on ZnFe2O4 catalyst. Int J Hydrog Energy 17:767–770

Lucas WY, Ji-Won M, Claudia JR, Lonnie JL, Adam JR, James RT, Bryan CC, Tommy JP (2011) Magnetic properties of bio-synthesized zinc ferrite nanoparticles. J Magn Magn Mater 323:3043–3048

Lv H, Ma L, Zeng P, Ke D, Peng T (2010) Synthesis of floriated ZnFe2O4 with porous nanorod structures and its photocatalytic hydrogen production under visible light. J Mater Chem 20:3665

Madubuonu N, Aisida SO, Ali A, Ahmad I, Ting-kai Z, Botha S, Maaza M, Ezema FI (2019) Biosynthesis of iron oxide nanoparticles via a composite of Psidium guavaja-Moringa oleifera and their antibacterial and photocatalytic study. J Photochem Photobiol B Biol 199:111601

Manjul G, Geeta J n P (2018) Synthesis and catalytic and biological activities of silver and copper nanoparticles using Cassia occidentalis. Int J Biomater 2018:6735426

McDonald KJ, Choi K-S (2011) Synthesis and photoelectrochemical properties of Fe2O3/ ZnFe2O4 composite photoanodes for use in solar water oxidation. Chem Mater 23:4863–4869

Mocherla PSV, Karthik C, Ubic R, Rao MSR, Sudakar C (2014) Effect of microstrain on the magnetic properties of BiFeO3 nanoparticles. Appl Phys Lett 105:132409

Monrudee L, Ranjan G, Puri IK (2011) Parametric investigation of heating due to magnetic fluid hyperthermia in a tumor with blood perfusion. J Magn Magn Mater 323:708–716

Mukherjee S, Mitra MK (2015) Effect of nickel ferrite on bismuth ferrite to generate nanocomposite in relation to structure, characterization, magnetic properties and band gap evaluation. Adv Mater Lett 6:902–906

Muscas G, Yaacoub N, Concas G, Sayed F, Sayed RH, Greneche JM, Cannas C, Musinu A, Foglietti V, Casciardi S, Sangregorio C, Peddis D (2015) Evolution of the magnetic structure with chemical composition in spinel iron oxide nanoparticles. Nanoscale 7:13576–13585

Nikam D, Jadhav S, Khot V, Bohara R, Hong C, Mali S, Pawar SH (2015) Cation distribution, structural, morphological and magnetic properties of Co1−xZnxFe2O4 (x = 0–1) nanoparticles. RSC Adv 5:2338

Nile S, Park SW (2013) Total phenolics, antioxidant and xanthine oxidase inhibitory activity of three colored onions (Allium cepa L.). Front Life Sci 7:224–228

Okoro DO, Ozuomba J, Aisida S, Asogwa P (2019) Thermal treated sysnthesis and characterization of polyethylene glycol (PEG) mediated Zinc ferrite nanoparticles. Surf Interface 16:127–131

Okoroh DO, Ozuomba JO, Aisida SO, Asogwa PU (2019) Properties of zinc ferrite nanoparticles due to PVP mediation and annealing at 500°C. Adv Nanopart 8:36–45

Otte J (1988) Hyperthermia in cancer therapy. Eur J Pediatr 147:560–569

Patrick B (1988) Magnetic surface anisotropy of cobalt and surface roughness effects within Neel's model. J Phys F 18:1291–1298

Raghvendra S, Ivo K, Jarmila V, Jaromir H, Jiri M, Lukas K, Jakub T, Jiří Š, Vojtěch E, Miroslava H (2017) Impact of grain size and structural changes on magnetic, dielectric, electrical, impedance and modulus spectroscopic characteristics of CoFe2O4 nanoparticles synthesized by honey mediated sol-gel combustion method. Adv Nat Sci Nanosci Nanotechnol 8:045002

Sagar ES, Patange S, Kadam R, Mane M, Jadhav K (2012) Structure refinement, cation site location, spectral and elastic properties of Zn2+ substituted NiFe2O4. J Mol Struct 1024:77–83

Sharifi I, Shokrollahi H, Amiri S (2012) Ferrite-based magnetic nanofluids used in hyperthermia applications. J Magn Magn Mater 324:903–915

Shete PB, Patil RM, Thorat ND, Prasad A, Ningthoujam RS, Ghosh SJ, Pawar SH (2014) Magnetic chitosan nanocomposite for hyperthermia therapy application: preparation, characterization and in vitro experiments. Appl Surf Sci 288:149–157

Tatarchuk TR, Paliychuk ND, Bououdina M, Al-Najar B, Pacia M, Macyk W, Shyichuk A (2018) Effect of cobalt substitution on structural, elastic, magnetic and optical properties of zinc ferrite nanoparticles. J Alloys Compd 731:1256–1266

Unchista W, Santi M, Ekaphan S (2016) EXAFS analysis of cations distribution in structure of Co1−xNixFe2O4 nanoparticles obtained by hydrothermal method in aloe vera extract solution. Appl Surf Sci 380:60–66

Van VM, De LAA, Raaymakers BW, Van MRJ, Hofman P, Lagendijk JJ, Battermann JJ (2004) Radiotherapy and hyperthermia in the treatment of patients with locally advanced prostate cancer. Preliminary results. BJU Int 93:36–41

Yang Y, Liu X, Yang Y, Xiao W, Li Z, Xue D, Lib F, Ding J (2013) Synthesis of nonstoichiometric zinc ferrite nanoparticles with extraordinary room temperature magnetism and their diverse applications. J Mater Chem C 1:2875–2885

Yu T, Shen Z, Shi Y, Ding J (2002) Cation migration and magnetic ordering in spinel CoFe2O4 powder: micro-Raman scattering study. J Phys Condens Matter 14:L613

Zhang C, Johnson DT, Brazel CS (2008) Numerical study on the multiregion bio-heat equation to model magnetic fluid hyperthermia (MFH) using low Curie temperature nanoparticles. IEEE Trans Nanobioscience 7(4):267–275

The main claim of the paper

Biogenic synthesis protocol for ZFNPs and AC-ZFNPs has been successfully obtained using AC as a biological reducing and capping agent for moderate hyperthermia property optimization. Optimized properties of the formulated samples were obtained by the AC concentrations which are propitious for hyperthermia application with moderate SAR values within the therapeutic range. The ZFNPs formulated are auspicious for hyperthermia applications with less side effect owing to their biocompatibility and moderate SAR value within the therapeutic range. The formulated nanoparticles have further broadened the horizon of moderate hyperthermia therapeutic applications with an innocuous protocol within 300 s.

Novelty

In this work, we have prepared ZFNPs functionalized with various concentrations of AC (20%, 40%, and 60%) by the biogenic method to enhance its biocompatibility. This method uses cost-effective, eco-friendly, and innocuous AC as a potential reducing agent to enhance the stability of the formulated colloidal solution for the first time. To our knowledge, the evaluation of the effects of AC on the properties of ZFNPs and its thermoablation evaluation has not been reported in the literature. Hence, the microstructural properties of the colloidal AC-ZFNPs were affirmed by SEM, TEM, and XRD. The optical properties were

evaluated by UV-Vis DRS and Raman spectral analyses; the magnetic properties were analyzed by VSM. The properties of ZFNPs were greatly enhanced by the concentration of AC. Also, the highest temperature and the specific absorption rate (SAR) for thermoablation were influenced by the concentration of AC. It is noteworthy that the influence of AC reduces the heating rate from 49 to 34 within 300 s to obtain the highest temperature within the therapeutic range. Hence, the properties of AC-ZnFNPs obtained are auspicious for thermoablation applications.

Why it is relevant

This research is relevant to alleviate the side effect of many cancer therapies such as chemotherapy and radiotherapy.

How the results advance the field

The self-heating of the formulated samples generates enough heating within the therapeutic temperature range 33–49 °C within 300 s to attain the highest temperature. This makes it a better candidate for magnetic hyperthermia applications. An increase in the concentration of AC atom reduces the heating temperature from 49 to 33 °C, to fall within the therapeutic range. Optimized properties of the formulated samples were obtained by the AC concentrations which are propitious for hyperthermia application with moderate SAR values within the therapeutic range. The obtained sample is projected for further in vivo and in vitro application in the future with thorough cytotoxicity assay.